

Spectra and dynamics of H₂ near the second dissociation threshold: Tunneling and Feshbach resonance

Yuan Yuan Han¹, Peng Wang, and Yuxiang Mo^{1*}*Department of Physics and State Key Laboratory of Low-Dimensional Quantum Physics, Tsinghua University, Beijing 100084, China* (Received 29 May 2022; accepted 12 July 2022; published 29 July 2022)

Both tunneling and Feshbach resonances occur near the second dissociation threshold of H₂. There are three channels, H(1s) + H(2p_{1/2}), H(1s) + H(2s_{1/2}), and H(1s) + H(2p_{3/2}), which correlate to the 2pσB¹Σ_u⁺, 3pσB¹Σ_u⁺, and 2pπC¹Π_u states, respectively. For the 2pπC state, there is a potential barrier near the dissociation limit, which accommodates bound states v' = 13, J' = 2, 3 with energies above the threshold. The tunneling dissociation results in H(1s) + H(2p_{3/2}), while Feshbach resonances produce H(1s) + H(2s_{1/2}) or H(1s) + H(2p_{1/2}). We measured the rotationally resolved spectra and determined the corresponding spectroscopic parameters. To study the dissociation dynamics, the spin-orbit branching ratios, and the fragment anisotropy parameters along the line profiles have been measured by a combination of Rydberg state ionization, velocity map ion imaging, and delay-time-curve methods. For the predissociation of the 2pπC¹Π_u⁺(v' = 13, J' = 2) state with fragment kinetic energy of 0.7 cm⁻¹, only the fragment H(2p_{1/2}) was observed. For the 2pπC¹Π_u⁻(v' = 13, J' = 3) state with fragment kinetic energy of 36 cm⁻¹, the branching ratio between H(2p_{1/2}) and H(2p_{3/2}) was found to be close to the diabatic limit, and the predissociation should occur via tunneling and coupling with a triplet state near the dissociation limit. For the 2pπC¹Π_u⁺, v' = 13, J' = 3 state, the predissociation should occur via tunneling, and coupling with the 3pσB¹Σ_u⁺ and 2pσB¹Σ_u⁺ states.

DOI: [10.1103/PhysRevA.106.012824](https://doi.org/10.1103/PhysRevA.106.012824)

I. INTRODUCTION

For molecular photodissociation, Feshbach resonance and tunneling (shape) dissociation may be classified into two types of predissociations [1–3]. Tunneling dissociation in an excited electronic state is usually accompanied by a Feshbach resonance. The simultaneous tunneling and Feshbach resonances involve two open channels and are different from Feshbach resonance, which involves couplings among closed and open channels. However, the two open channel coupling problem is common in molecular photodissociation and is more complicated than the Feshbach resonance.

For one photon photodissociation of H₂ near the second threshold, there are three channels, H(1s) + H(2p_{1/2}), H(1s) + H(2s_{1/2}), and H(1s) + H(2p_{3/2}), that correlate to the 2pσB¹Σ_u⁺, 3pσB¹Σ_u⁺, and 2pπC¹Π_u states, respectively [4–15]; see Fig. 1 for the related potential energy curves. It is known that there is a potential barrier for the 2pπC¹Π_u state due to the avoided crossing of the same symmetric electronic states [4–17]. Several rotational states of 2pπC¹Π_u(v' = 13) have been found with energies above the dissociation threshold [4,12–19].

In 1998, Cheng *et al.* measured the line profile for the transition to the 2pπC¹Π_u⁺(v' = 13, J' = 3) state [4]. The measured linewidth was found to be much larger than that of theoretical calculations that considered the adiabatic coupling between the 2pσB¹Σ_u⁺ and 2pπC¹Π_u states and the tunneling dissociation [16]. The rotationally resolved line profiles for other transitions have not been reported, and the

energy levels for the 2pπC¹Π_u[±](v' = 13, J' = 2, 3) states have different reported values [4,12–19]. These unresolved issues were attributed to the overlapping of various rotational transitions near the threshold, including below and above the threshold states. It is one of our motivations to develop experimental methods to deconvolute these blended lines and provide better spectroscopic parameters. In the case of D₂, it is fortunate that the resonance lines near the threshold are not blended and have been analyzed [4,10–14].

In addition to the line profiles, fragment state distributions should provide further insight into the spectra and predissociation dynamics. Recently, we measured dissociation channel branching ratios D(1s) + D(2s), D(1s) + D(2p_{1/2}), and D(1s) + D(2p_{3/2}) produced from the tunneling dissociation of D₂ by using a combination of Rydberg state ionization, velocity map imaging, and delay-time-curve detection of D(2s, 2p) fragments [10,11]. The results indicated that simultaneous shape and Feshbach resonances occur in D₂. Because of the small spin-orbit splitting relative to the fragment kinetic energies, the spin-orbit branching ratios approach the diabatic coupling limit [2,11].

It is worth noting that the rotational state 2pπC¹Π_u⁺(v' = 13, J' = 2) of H₂ is only 0.7 cm⁻¹ above the threshold, which is comparable to the spin-orbit splitting of 0.36 cm⁻¹ [4,12–17]. Therefore, the diabatic model may not be suitable for describing the population distribution of the spin-orbit states, which provides us a good opportunity to study the relative importance between the shape and Feshbach resonances.

Recently, we found that the variation in anisotropy parameters along the line profile, which we call the β profile, is a useful tool to study the state coupling dynamics in a single

*Correspondence: yimo@mail.tsinghua.edu.cn

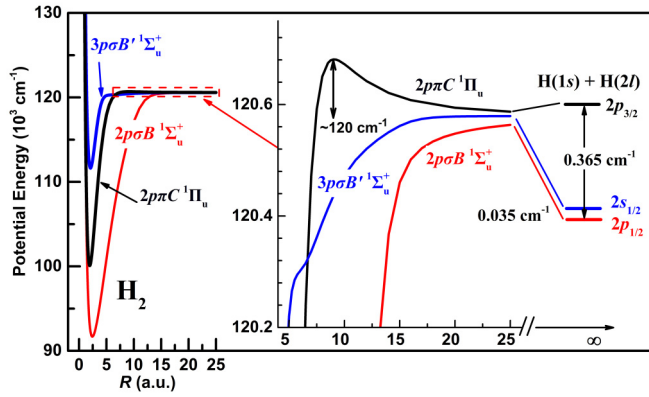


FIG. 1. Potential energy curves of H_2 correlating to the second dissociation limit. The inset shows the potential barrier in the $2p\pi C^1\Pi_u$ state [15].

isolated Feshbach resonance [20–25]. Although the simultaneous shape and Feshbach resonances involve two open channels, it would be interesting to see if the β profile could give us new insight into the state coupling dynamics.

In this paper, we reported the rotationally resolved line profiles due to the predissociation of H_2 near the second dissociation threshold by decoupling the signals from the dissociative ionization and other overlapped transitions. We also determined the spin-orbit branching ratios using the Rydberg state ionization technique. It is interesting to find that only the $H(1s) + H(2p_{1/2})$ channel or the Feshbach resonance was observed for the resonance state with energy 0.7 cm^{-1} above the threshold. However, for resonance states with energies 36 cm^{-1} above the threshold, the channel branching ratios between $H(1s) + H(2p_{1/2})$ and $H(1s) + H(2p_{3/2})$ approach the diabatic limit. The measured β profiles are found to provide valuable insights into the predissociation dynamics.

II. EXPERIMENTS

Our experimental setup has been described in previous publications [10,11,23–27], and only a summary is given here. The setup consists of a tunable XUV pump laser (84.4–85.1 nm), a probe laser (at 656 or 365 nm), and a typical molecular beam machine equipped with a velocity map imaging component [28]. The XUV laser was generated by a four-wave sum frequency mixing method using one fixed frequency laser, one tunable laser, and one pulse Kr jet as the nonlinear medium. A toroidal grating was used to separate the fundamental laser beams from the XUV laser beam and to focus the XUV beam on the H_2 beam. The wavelengths of the two fundamental laser beams were calibrated by a commercial wavemeter, WS-6 (HighFinesse Corp., Germany). Because the dissociation threshold of H_2 is very accurate, we also checked our XUV wavelength using the dissociation threshold in the spectra.

A. Measurement of branching ratio $[H(2s)]/[H(2s) + H(2p)]$

The $H(2s, 2p)$ signals were measured as a function of delay times between the XUV pump laser and the UV probe laser pulses under field-free conditions [10,11,23–27]. A

pulsed electric field was applied about 200 ns after the pump laser pulse to extract the H^+ ions. The focused UV probe laser (364 nm, 1 mJ/pulse, $f = 300\text{ mm}$) ionized the $H(2s, 2p)$ fragments. The ionization rate is much larger than the fluorescence rate of the $H(2p)$ atom. We refer to the measured curve as the delay-time curve.

Since the lifetimes of the $H(2s)$ (0.12 s) and $H(2p)$ (1.6 ns) states are very different and the pulse widths of both the XUV pump and UV probe lasers are 6 ns, the signals measured at 15 ns after the XUV pump laser pulses should be from the $H(2s)$ fragments, and the signals measured with zero delay time are a summation of the $H(2s)$ and $H(2p)$ fragments. Thus, the branch ratio ($[H(2s)]/[H(2s) + H(2p)]$) can be determined.

B. Measurement of spin-orbit branching ratio $[H(2p_{3/2})]/[H(2p_{1/2}) + H(2p_{3/2})]$

The photodissociation experiments were performed under field-free conditions, and the fragments $H(2s, 2p)$ were excited to high-lying Rydberg states $H(nl, n = 30\text{--}60)$ by a probe laser ($\sim 365\text{ nm}$) pulse in coincidence with the XUV laser pulse. The $H(nl)$ fragments were ionized by a delayed (200 ns) pulsed electric field relative to the XUV laser pulse [11]. We call this detection method the Rydberg state ionization method (RSI). By recording the H^+ signal intensity as a function of the probe laser frequencies, we obtained a spectrum of the Rydberg state series, called the RSI spectrum.

Note that the $H(2s_{1/2})$ and $H(2p_{1/2,3/2})$ components are present in the RSI spectrum mentioned above. An RSI spectrum with only the $H(2s)$ components can be measured by delaying the probe laser 40 ns relative to the XUV laser pulse (referred to as the RSID spectrum). The RSI spectrum with only the $H(2p_{1/2,3/2})$ components can be obtained by subtracting the RSID spectrum from the RSI spectrum of $H(2s_{1/2}, 2p_{1/2,3/2})$. To avoid broadening the RSI and RSID spectra by the Stark effect, great care was taken to make the residual electric field in the vacuum chamber as weak as possible.

For Rydberg states with $n > 30$, the spin-orbit splittings ($< 10^{-4}\text{ cm}^{-1}$) can be neglected relative to the probe laser resolution ($\sim 0.1\text{ cm}^{-1}$). Therefore, all spin-orbit states of the same nl are summed in the RSI spectrum. It is easy to show that the line intensities of the $2p_{3/2}$ and $2p_{1/2}$ states are equal in the RSI spectrum for a particular nl state [11]. By calculating the relative intensities in the spin-orbit state resolved RSI spectrum, the branching ratios between $H(2p_{3/2})$ and $H(2p_{1/2})$ can be determined.

C. Velocity map images of the fragments $H(2l)$, $H(2p_{3/2})$, and $H(2p_{1/2})$

The velocity map images of the $H(2l, l = s, p)$ fragments were measured under an electric field ($\sim 300\text{ V/cm}$), in which the $H(2s)$ and $H(2p)$ states were completely mixed [29].

The state-resolved velocity map images of the $H(2s_{1/2})$, $H(2p_{2/3})$, and $H(2p_{1/2})$ fragments must be obtained under field-free conditions. The velocity map images of the $H(2p_{3/2})$ fragments were obtained under field-free conditions

with the probe laser frequency fixed at the center of the $2p_{3/2}$ peak in the RSI spectrum. However, the peaks of $2s_{1/2}$ and $2p_{1/2}$ in the RSI spectrum overlap severely because the energy spacing between the two is small ($\sim 0.03 \text{ cm}^{-1}$). We measured the $\text{H}(2s_{1/2}, 2p_{1/2})$ and $\text{H}(2s_{1/2})$ fragment images under field-free conditions, respectively. For the $\text{H}(2s_{1/2})$ image, a probe laser delay of 40 ns relative to the pump laser pulse was applied. The velocity map images of the $2p_{1/2}$ state can thus be obtained by the difference between the two images.

The angular distribution of the photofragments can be determined from the velocity map images and are fitted using the well-known formula [30]

$$f(\theta) \propto 1 + \beta P_2(\cos \theta), \quad (1)$$

where θ is the angle between the recoil velocity vector and the polarization direction of the dissociation laser, and $P_2(\cos \theta)$ is the second-order Legendre polynomial. β is the so-called anisotropy parameter.

III. EXPERIMENTAL RESULTS

Figure 2(a) shows the $\text{H}(2l)$ fragment yield spectrum and photoexcitation spectrum of H_2 under an electric field (dc). The $\text{H}(2l)$ fragments were detected using the so-called one-photon resonance-enhanced one-photon ionization method, often denoted as (1 + 1) REMPI, with the resonance transition between the $\text{H}(2l)$ and $\text{H}(3l)$ (Balmer α line, 656.3 nm) states. The excited states of H_2 were also ionized by the same probe laser. Since the photon energy of the probe laser (1.89 eV) plus that of the XUV laser ($\sim 14.68 \text{ eV}$) was lower than the threshold (18.08 eV) of dissociative ionization of the H_2 molecule, the H^+ signals could not be from the one-photon dissociative ionization of H_2^* and should be from the photoionization of the $\text{H}(2l)$ fragments. Figure 2(b) shows the $\text{H}(2s)$ yield spectra and excitation spectra of H_2 measured under the field-free condition with the probe (ionization) laser delayed 40 ns (referred to as the FFD method).

The spectra in the energy region shown in Fig. 2(a) can be assigned from the transitions to the $2p\sigma B^1\Sigma_u^+$, $3p\sigma B'^1\Sigma_u^+$, and $2p\pi C^1\Pi_u$ states. We only labeled the rotational lines of

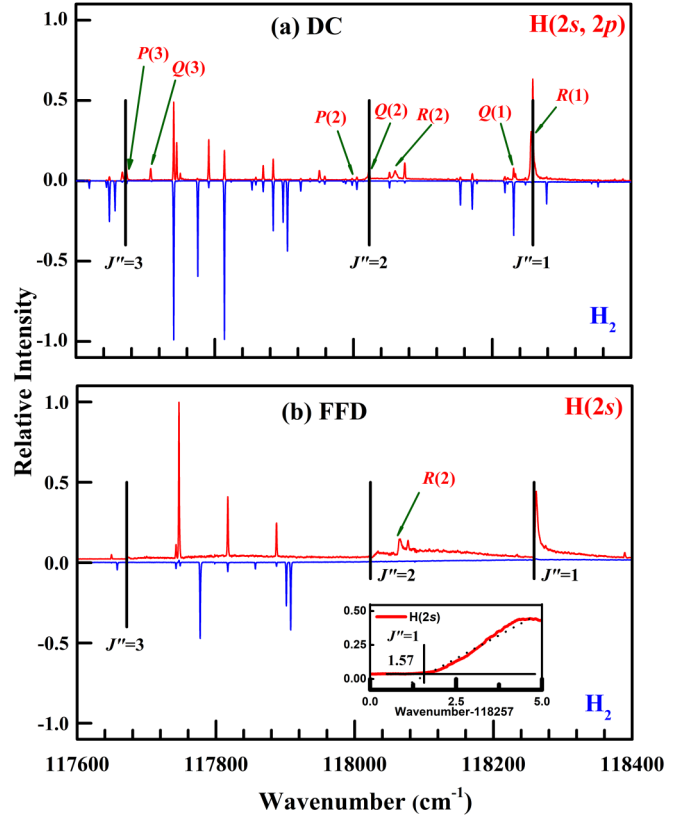


FIG. 2. (a) The $\text{H}(2l)$ fragment yield spectrum and the photoexcitation spectrum of H_2 measured simultaneously with the pump and probe laser (656.3 nm) pulses overlapping in time under the electric field (dc); (b) the corresponding spectra measured under the field-free condition with the probe laser pulse delayed 40 ns relative to the pump laser pulse (FFD). The black vertical lines show the dissociation thresholds for the initial rotational states of H_2 . Rotational assignments are for the transitions to $2p\pi C^1\Pi_u(v' = 13)$, and the line positions are listed in Table I.

$2p\pi C^1\Pi_u$ that we were interested in. The dissociation thresholds for the initial rotational states of $J'' = 1, 2, \text{ and } 3$ were

TABLE I. Line positions ω_0 , linewidths Γ , available energy E_t , branching ratios $\alpha = [\text{H}(2s)]/[\text{H}(2s) + \text{H}(2p)]$, $\delta = [\text{H}(2p_{3/2})]/[\text{H}(2p_{3/2}) + \text{H}(2p_{1/2})]$, and the $\text{H}(2s_{1/2}, 2p_{1/2,3/2})$ fragment anisotropy parameters β from the predissociations of the $2p\pi C^1\Pi_u(v' = 13)$ state. The uncertainties of ω_0 , Δ , and E_t are 0.1 cm^{-1} . The uncertainties of Γ for the $Q(2)$, $R(1)$, and $P(3)$ transitions are estimated as 0.02 cm^{-1} , and for $Q(3)$ and $R(2)$ are 0.1 cm^{-1} .

Transition	$\omega_0 \text{ (cm}^{-1}\text{)}$		$E_t \text{ (cm}^{-1}\text{)}^b$	$\Gamma \text{ (cm}^{-1}\text{)}$		q^c	α	δ	β^d			
	This work	Ref. [4]		Ref. [13]	This work				Ref. [4]	$2p_{3/2}$	$2p_{1/2}$	$2s_{1/2}$
$Q(2)$	118023.1	-0.1	1.4	0.5	0.57	50 ± 5	<0.1					
$R(1)$	118259.2	-3.0	-1.3	0.7	0.54	0.4	>100	<0.1	0.0			
$P(3)$	117672.4	-2.8		0.9	0.65		<-100	<0.1	0.0			
$Q(3)$	117707.4		-0.2	36.0	1.3		>20	<0.01	0.63	-0.59	-0.67	-0.68
$R(2)$	118059.9	0.1	-2.1	37.3	4.5	3.56	>50	0.46		0.81	1.34	0.08

^aThe difference between this work and references.

^bAvailable energy for the fragments. The threshold of $\text{H}(1s) + \text{H}(2p_{1/2})$ is $118376.98 \text{ cm}^{-1}$ [8]. The rotational energies for the ground state of H_2 are $118.50, 354.39, \text{ and } 705.54 \text{ cm}^{-1}$ for $J' = 1, 2, \text{ and } 3$, respectively [14].

^cThe Fano q parameters for the $Q(3)$ and $R(2)$ transitions are only semiquantitative.

^dUncertainty is estimated as 0.02.

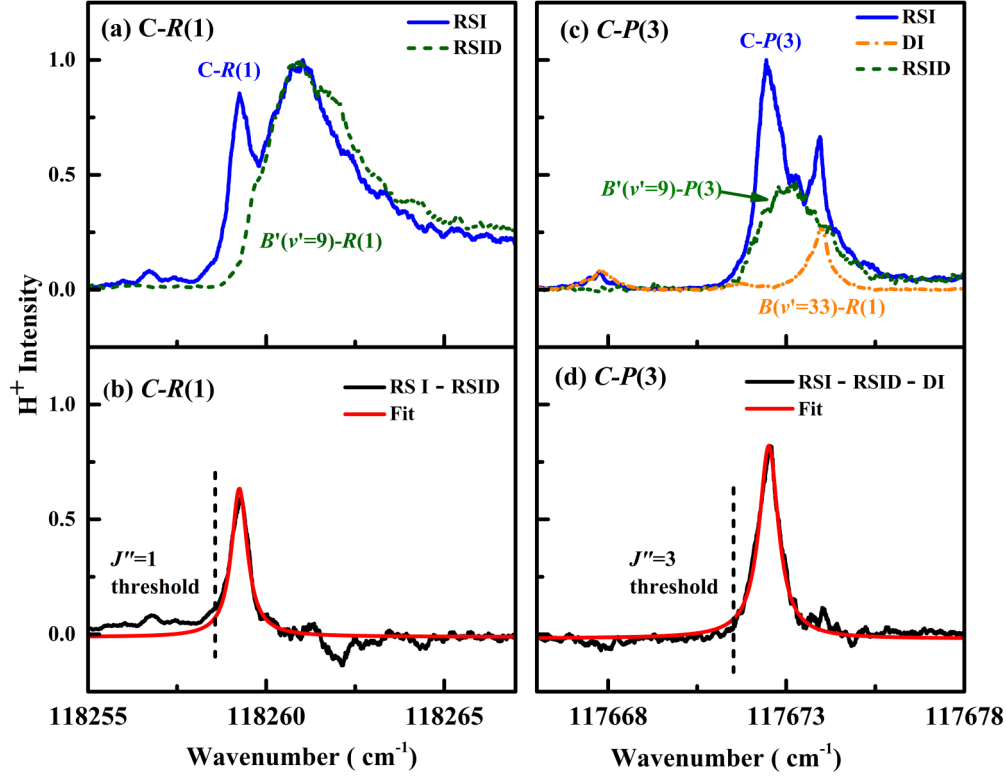


FIG. 3. (a) The spectra of the $R(1)$ transition to $2p\pi C^1\Pi_u^+(\nu' = 13, J' = 2)$ measured using the RSI and RSID detection methods (see Sec. II B). The probe laser pumped $H(2p_{1/2})$ to $H(nl, n = 46)$; (b) the rotationally resolved $R(1)$ spectrum in the black (fluctuated) line obtained by the difference of the two spectra showing in panel (a), and the red (smooth) line is the fit; (c) the spectra of the $P(3)$ transition. The probe laser frequency was fixed at the peak of the transition $H(n = 37) \leftarrow H(2p_{1/2})$ in the RSI and RSID spectra. The orange dotted dash curve represents the H^+ signals from the dissociative ionization (DI) of H_2^+ with the probe laser fixed at a frequency between peaks $H(n = 37)$ and $H(n = 38)$ in the RSI spectrum; (d) the black (fluctuated) line is the $P(3)$ spectrum obtained by subtracting the spectra using the RSID and DI detection methods from the spectrum using the RSI method. The red (smooth) line is the fit. The fit parameters are listed in Table I.

easily identified. The inset in Fig. 2(b) shows the threshold for $J'' = 1$.

By comparison between Figs. 2(a) and 2(b), it is seen that the Q branches almost disappeared using the FFD method. The results showed that the Q branches correlate to the dissociation channel of $H(1s) + H(2p)$, which is in agreement with the previous results [10,11,23–25]. The reason is that the Q branches are the transitions to the $2p\pi C^1\Pi_u^-$ state that cannot interact with the $3p\sigma B'^1\Sigma_u^+$ state correlating to the channel $H(1s) + H(2s)$ due to the symmetry requirement.

For a single isolated Feshbach resonance, the line profile can be fitted using the so-called Fano formula [1–3,31],

$$\sigma(\omega) = \sigma_i \frac{[q + 2(\omega - \omega_0)/\Gamma]^2}{1 + [2(\omega - \omega_0)/\Gamma]^2} + \sigma_b, \quad (2)$$

where σ_i and σ_b represent the absorption cross sections to the interacting and noninteracting continuum states, respectively. q is the Fano parameter, ω_0 , the resonance frequency, and Γ , the linewidth. We neglected σ_b in the fits.

A. State-resolved spectra for the $2p\pi C^1\Pi_u^\pm(\nu' = 13, J' = 2)$ state

To obtain the state-resolved spectrum, we must subtract the components interfering with the target spectrum from the total

spectrum. To cross-examine the results, we determined the spectroscopic parameters using the $R(1)$ and $P(3)$ transitions. The related spectra are shown in Figs. 3(a)–3(d).

1. Rotational-state-resolved spectrum of the $R(1)$ transition

The XUV fluorescence-excitation spectrum of the H_2 molecule and the $H(2s)$ fragment yield spectrum were recorded near the $R(1)$ transition by Balakrishnan *et al.* in 1992 [7]. Two peaks overlapped heavily in the spectrum. One peak was associated with the dissociation channel $H(1s) + H(2s)$ and the other with $H(1s) + H(2p)$. In 1998, Cheng *et al.* obtained a similar fragment yield spectrum by exciting the H_2 molecule using a two-step photoexcitation process and multiphoton ionization of $H(2l)$ fragments [4]. Cheng *et al.* assigned the first peak as the $R(1)$ transition to $C^1\Pi_u(\nu' = 13, J' = 2)$, and the second peak as the $R(1)$ transition to $3p\sigma B'^1\Sigma_u^+(\nu' = 9, J' = 2)$ that correlates to the channel $H(1s) + H(2s)$ [4].

Figure 3(a) shows the $H(2s, 2p)$ and $H(2s)$ fragment yield spectra near the second threshold of $H_2(J'' = 1)$ detected using the RSI and RSID methods, respectively. Note that the probe laser was a collimated UV (365 nm) laser beam in this case. The spectrum confirms the previous results, namely, that the first peak is associated with $H(1s) + H(2p)$ and the second peak with $H(1s) + H(2s)$. Subtracting the spectrum of

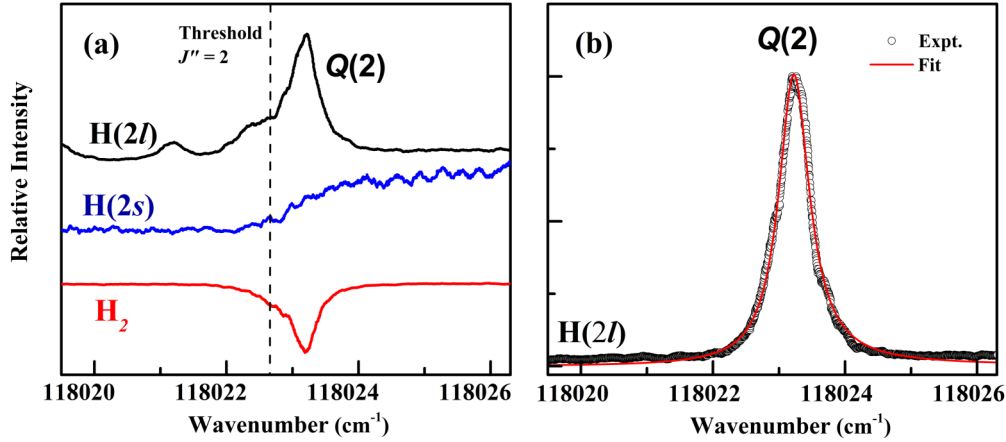


FIG. 4. The spectrum of the $Q(2)$ transition to $2p\pi C^1\Pi_u^-(v' = 13, J' = 2)$. (a) The $H(2l)$ fragment yield and H_2 excitation spectra measured under field-free condition with the pump and probe laser coincidence in time, and the $H(2s)$ fragment yield spectrum measured with the probe laser delayed 40 ns relative to the pump laser. (b) The spectrum measured by recording the signals of near-zero kinetic energies of the $H(2l)$ fragments [33,34]. The signal intensities are not scaled in the figure.

the $H(2s)$ fragments from that of the $H(2s, 2p)$ fragments, we obtained the rotational-state-resolved $R(1)$ spectrum as shown in Fig. 3(b). As can be seen, the line profile is relatively symmetrical. The fit parameters can be found in Table I.

2. Rotational-state-resolved spectrum of the $P(3)$ transition

Similar to the studies for the $R(1)$ transition, we measured the yield spectra of the $H(2l)$ and $H(2s)$ fragments near the dissociation threshold of $H_2(J'' = 3)$, as shown in Fig. 3(c). There are three overlapped peaks in total. As mentioned in Sec. III A 1, the $P(3)$ transition to $3p\sigma B^1\Sigma_u^-(v' = 9, J' = 2)$ produces only $H(2s)$ fragments. There are also H^+ signals from the dissociative ionization of $H_2(2p\sigma B^1\Sigma_u^+, v' = 33, J' = 2)$ excited by the $R(1)$ transition. The corresponding H_2 excitation spectrum can be found in Fig. S1 in the Supplemental Material [32]. The H^+ signals from the dissociative ionization, as shown by the dotted dash line (orange) in Fig. 3(c), were measured by tuning the probe laser off the line centers of the peaks in the RSI spectrum. The rotational state-resolved spectrum for the $P(3)$ transition was thus obtained by subtracting the $H(2s)$ yield spectrum measured using the RSID method and the H^+ dissociative ionization (DI) spectrum from the $H(2l)$ yield spectrum measured using the RSI method, as shown in Fig. 3(d). The fit parameters are listed in Table I.

Table I shows that the linewidths and energy levels of the $R(1)$ and $P(3)$ transitions are in reasonable agreement considering that the two state-resolved spectra were obtained indirectly. The average value of the energy level $J' = 2$ is thus $118\,377.8 (\pm 0.1) \text{ cm}^{-1}$, lower than the $118\,380.7 \text{ cm}^{-1}$ reported by Cheng *et al.* [4], but higher than $118\,374.63 \text{ cm}^{-1}$ reported by Abgrall *et al.* [17]. The average linewidth is $0.60 (\pm 0.05) \text{ cm}^{-1}$.

3. Rotational-state-resolved spectrum of the $Q(2)$ transition

Figure 4(a) shows the $H(2l, l = s, p)$ and $H(2s)$ fragment yield spectra near the second threshold of $H_2(J'' = 2)$, which were measured under field-free conditions with the probe laser

(364 nm, 1 mJ/pulsed, $f = 300$ mm) without delay, and with a 40 ns delay relative to the pump laser pulses, respectively. The excitation spectrum of H_2 obtained by ionization of H_2^* using the same UV probe laser is also shown in Fig. 4(a). A similar H_2 excitation spectrum was reported by Cheng *et al.* using multiphoton ionization of H_2^* ; however, they did not report the $H(2l)$ fragment yield spectra [4].

There were at least two overlapped peaks in the $H(2l)$ fragment yield spectrum measured under the field-free condition. The left peak correlates to the $H(1s) + H(2p)$ channel, as evidenced by the $H(2s)$ spectra. This peak should come from $J'' = 3$ since it is located below the threshold of $J'' = 2$ and is predissociated (the population of $J'' = 4$ could be neglected in our H_2 beam); however, its exact assignment is not known to us. The right peak was assigned as $Q(2)$ by Cheng *et al.* [4]. The $Q(2)$ peak correlates to the $H(1s) + H(2p)$ channel and is located about 0.5 cm^{-1} above the threshold of $J'' = 2$. Because of the near-zero kinetic energy of the fragments, we could distinguish $Q(2)$ from its neighbor peak with $J'' = 3$ by using a technique similar to the zero-kinetic-energy photoelectron spectroscopic method [33,34]. Therefore, a spectrum with only the $Q(2)$ transition was obtained and is shown in Fig. 4(b). The fit parameters for this peak are shown in Table I.

The energy level for $C^1\Pi_u^-(v' = 13, J' = 2)$ is thus $118\,377.5 \text{ cm}^{-1}$, in agreement with the reported value [4]. The energy difference between $C^1\Pi_u^+(v' = 13, J' = 2)$ and $C^1\Pi_u^-(v' = 13, J' = 2)$ is determined to be $0.3 (\pm 0.1) \text{ cm}^{-1}$, which is in agreement with the value of 0.47 cm^{-1} reported by Abgrall [17].

B. State-resolved spectra for the $2p\pi C^1\Pi_u^\pm(v' = 13, J' = 3)$ states

Figures 5(a) and 5(b) show the $H(2l)$ fragment yield spectra and the H_2 excitation spectra for the $Q(3)$ and $R(2)$ transitions, respectively. There were H_2^+ signals observed in the $Q(3)$ transition, which indicated that some of the observed H^+ signals were from the dissociative ionization of H_2^* induced by the focused probe laser (364 nm). The line center of the $Q(3)$ branch is $117\,707.4 (\pm 0.1) \text{ cm}^{-1}$, which is very close

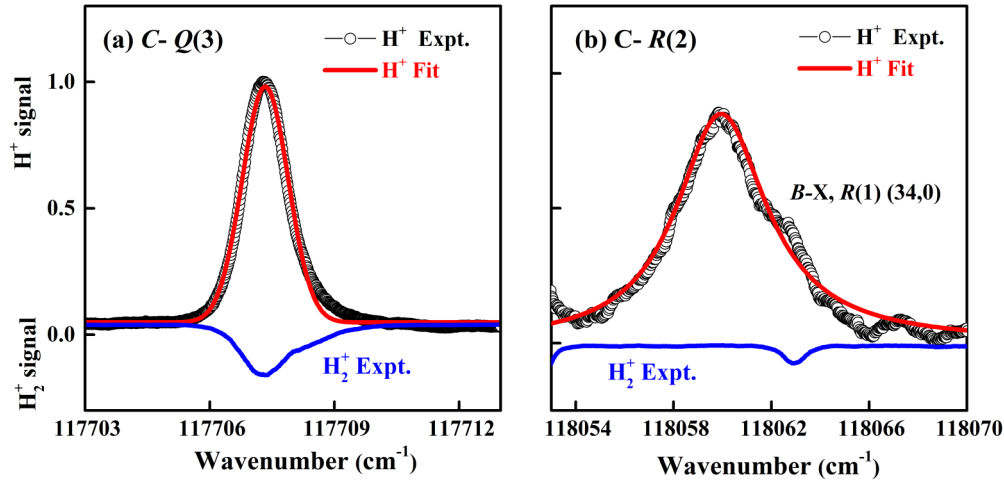


FIG. 5. The $H(2l)$ fragment yield spectra (open cycle) and H_2 excitation spectrum (lower blue line) from the (a) $Q(3)$, and (b) $R(2)$ transitions to $2p\pi C^1\Pi_u(v' = 13)$ under electric field. The solid red line is the nonlinear least-squares fits using the Fano formula.

to the value of $117\,707.57$ reported by Namioka [13]. The line center of the $R(2)$ branching is $118\,059.9\text{ cm}^{-1}$, which is good agreement with that of Cheng *et al.* [4], but different from the $118\,061.96\text{ cm}^{-1}$ of Namioka [13].

The linewidth of the $Q(3)$ transition is $1.3 (\pm 0.1)\text{ cm}^{-1}$, which is consistent with the fact that the excited H_2^* was observed with a focused probe laser beam. The linewidth of the $R(2)$ transition is $4.5 (\pm 0.1)\text{ cm}^{-1}$. There was no H_2^+ signal observed due to the short lifetime of the excited H_2^* [small H_2^+ signals were observed; however, they were from the $R(1)$ transition to $2p\sigma B^1\Sigma_u^+(v' = 34)$]. It is interesting to note that neither line profile could be satisfactorily fitted using the Fano formula [Eq. (2)]. This is probably because the dissociations involve two open channels [$H(1s) + H(2p_{1/2,3/2})$], which cannot be described by Eq. (2) [3].

Note that both the $Q(3)$ and $R(2)$ transitions have larger linewidths than those of the $Q(2)$ and $P(3)$ transitions, which indicates that they have stronger L -uncoupling strengths.

C. Branching ratios of $[H(2s)]/[H(2s) + H(2p)]$

Figure 6 shows the measured delay-time curves for the $Q(3)$, $R(2)$, and $P(3)$ transitions. As we mentioned (see Fig. 1), channel $H(1s) + H(2s)$ correlates to the $3p\sigma B^1\Sigma_u^+$ state, while channel $H(1s) + H(2p)$ correlates to the $2p\pi C^1\Pi_u$ and $2p\sigma B^1\Sigma_u^+$ states.

For the $Q(3)$ transition, the experimental results demonstrated that only the $H(2p)$ fragments were produced, as we mentioned earlier. For the $R(2)$ transition, Fig. 6(b) indicates that there is a large percentage (46%) of the $H(2s)$ components present, which indicates that the corresponding predissociation involves direct or indirect couplings between $2p\pi C^1\Pi_u^+$ with $3p\sigma B^1\Sigma_u^+$. The previous theoretical calculation did not take this coupling into account, which may be the reason why the calculated linewidths ($<0.1\text{ cm}^{-1}$) were much smaller than the experimental results [16].

For the $P(3)$ transition, it seems that there were $\sim 10\%$ $H(2s)$ components. However, there were some $H(2s)$ signals from the overlapping $P(3)$ transition to

$3p\sigma B^1\Sigma_u^+(v' = 9, J' = 2)$ [4], as shown in Fig. 3(c). It is thus expected that the $H(2s)$ fragments produced in the $P(3)$ transition should be much less than 10%.

For the $Q(2)$ and $R(1)$ transitions, the delay-time curve could not provide qualitative branching ratios of $[H(2s)]/[H(2s) + H(2p)]$ because of the $H(2s)$ fragments produced from the direct dissociations of the molecules with $J'' = 3$ in the H_2 beam [27,35]. However, the branching ratios are less than 10%, as seen in Fig. 2(b), which is consistent with the previous results [4].

D. Spin-orbit branching ratio $[H(2p_{1/2})]/[H(2p_{1/2}) + H(2p_{3/2})]$

Figure 7(a) shows the RSI and RSID spectra of the $P(3)$ transition, and Fig. 7(b) shows those of the $R(1)$ transition. We introduced the RSI and RSID spectra in Sec. II B. The RSI and RSID spectra were alternatively measured. As seen from the insets shown in Figs. 7(a) and 7(b), no $H(2p_{3/2})$ component was found in the RSI spectra. Note that the $H(2s_{1/2})$ components were mainly from the overlapping transitions [see Fig. 3(c)] and background dissociations [27,35]. Therefore, only the $H(2p_{1/2})$ component was observed in the $P(3)$ and $R(1)$ transitions.

Figure 8(a) shows the RSI and RSID spectra of the $H(2l)$ fragments produced from the $Q(3)$ transition of $2p\pi C^1\Pi_u(v = 13)$. Figure 8(b) shows an expanded spectrum of $H(nl, n = 37)$, which demonstrates that both $H(2p_{3/2})$ and $H(2p_{1/2})$ components are present. The branching ratio $[H(2p_{1/2})]/[H(2p_{1/2}) + H(2p_{3/2})]$ was calculated by the relative areas between the two components in the difference spectra between RSI and RSID [11]. The statistical average of all peaks yields a value of $0.63(\pm 0.03)$, approaching the diabatic ratio of $2/3$; see also Table S1 in the Supplemental Material [32]. Note that in the diabatic model, the spin-orbit branching ratios are determined by the components of spin-orbit states in the diabatic states [2].

For the $R(2)$ transition, due to the strong $H(2s)$ signals, we have not obtained a reliable spin-orbit branching ratio.

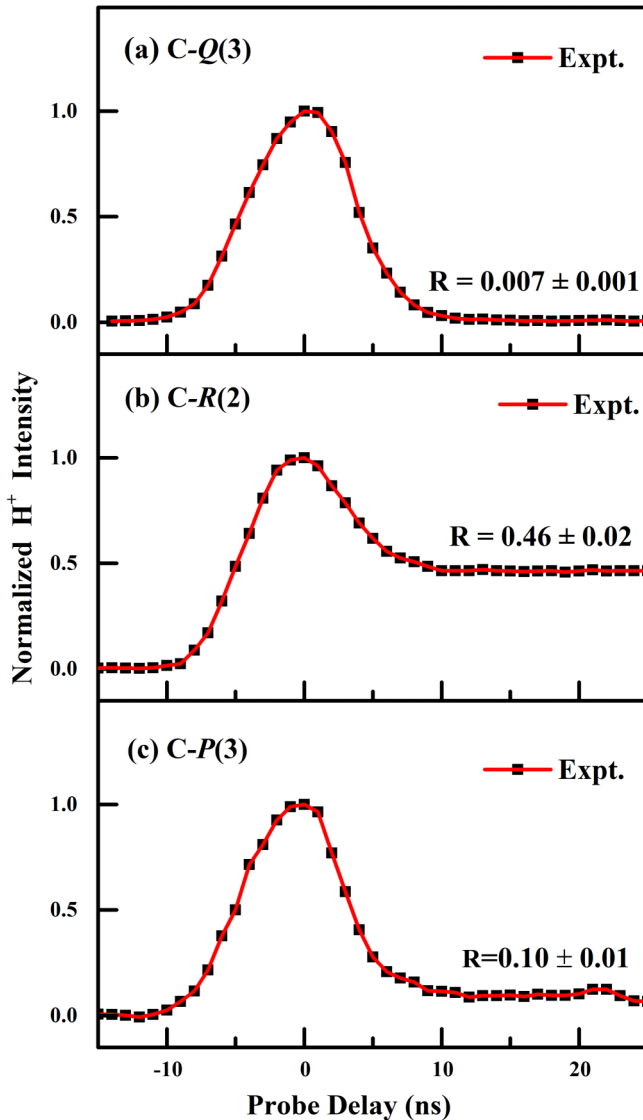


FIG. 6. The delay-time curves for the determination of branching ratios $[H(2s)]/[H(2s) + H(2p)]$ for the predissociations due to (a) $Q(3)$, (b) $R(2)$, and (c) $P(3)$ transitions to $2p\pi C^1\Pi_u(v' = 13)$.

E. State-resolved fragment angular distributions for the $Q(3)$ and $R(2)$ transitions

Figure 9 shows the inverse-Abel transforms of the velocity map images of the spin-orbit state resolved $H(2l)$ fragments produced from the $Q(3)$ and $R(2)$ transitions. The corresponding angular distributions are also shown in the figure.

For the $Q(3)$ transition, the anisotropy parameters of $H(2p_{1/2})$ and $H(2p_{3/2})$ were determined to be -0.67 and -0.59 , respectively, which are similar to the theoretical value of -0.75 assuming a dissociating state of $^1\Pi_u$ symmetry [19,25]. The agreement between the experimental values and the theoretical model may indicate that the predissociation occurs via the tunneling dissociation mechanism; however, the observed spin-orbit branching ratio of $2/3$ suggests that both tunneling and coupling with another state (see the following discussion) should play roles in the predissociation. This contradiction can be understood as the angular distribution of the

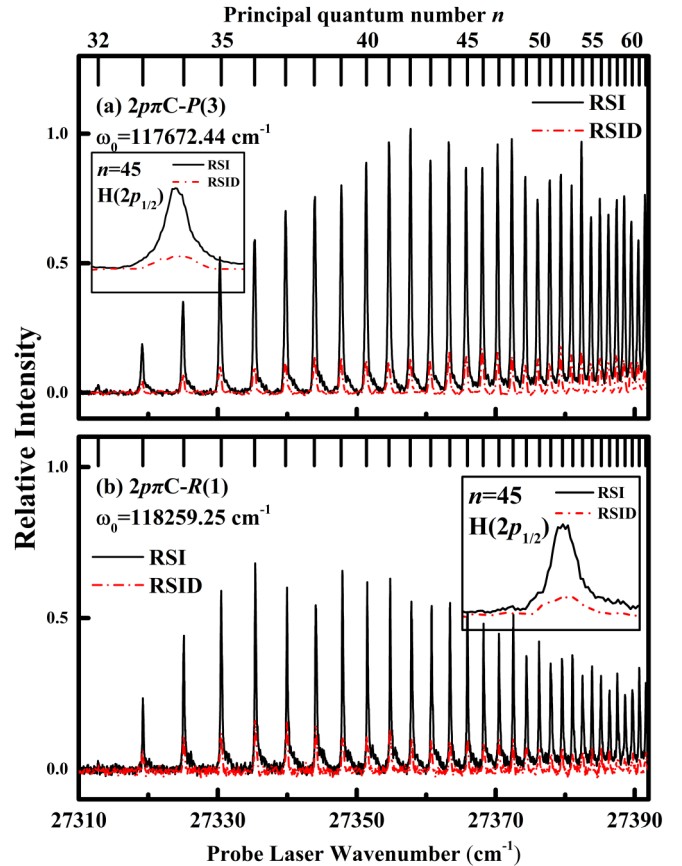


FIG. 7. The RSI and RSID spectra of the $H(2l)$ fragments produced from the predissociations due to (a) $P(3)$, and (b) $R(1)$ transitions to $2p\pi C^1\Pi_u^+(v' = 13)$. The insets in the figure show that no $H(2p_{3/2})$ fragments were produced in the predissociations.

fragments being determined primarily by the transitions in the Franck-Condon region, while the spin-orbit state distribution is determined primarily by the state coupling near the dissociation limits [11].

For the $R(2)$ transition, the anisotropy parameters of the $H(2p_{3/2})$ and $H(2p_{1/2})$ fragments were determined to be 0.81 and 1.34 , respectively. The theoretical β value of the $R(2)$ transition with a dissociating state of $^1\Sigma_u^+$ symmetry is 0.8 [26]. Although the β value of the $H(2p_{3/2})$ fragment agrees with a dissociating state of $^1\Sigma_u^+$ symmetry, the β value of the $H(2p_{1/2})$ fragment is larger than that of the theoretical model, which we do not yet understand. Note that without the state-resolved β value of $H(2l)$ is 0.74 in agreement with the theoretical model.

F. β profiles of the $Q(3)$ and $R(2)$ transitions

The β values for a predissociation usually vary along the absorption line profile, which we call the β profile [20–25]. For a Feshbach resonance, the absorption intensity at the line center is mainly due to the quasibound state, and β at the line center can be calculated using a simple analytical formula [20,26]. As the excitation energy deviates from the center, it is also possible to calculate β using a theoretical model [20–25]; however, several dynamical parameters are involved.

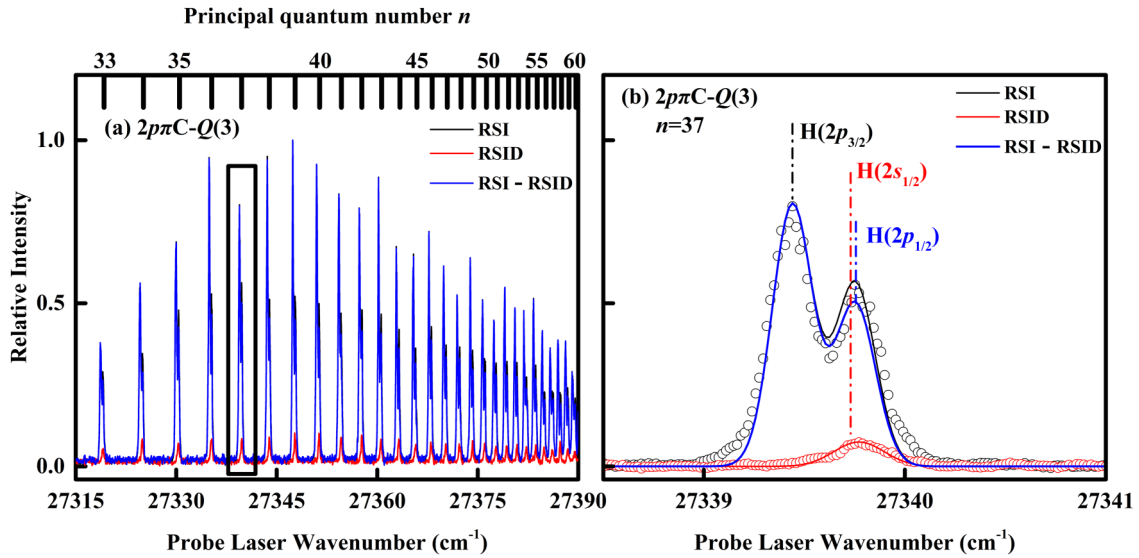


FIG. 8. (a) The RSI and RSID spectra of the H(2l) fragments produced from the predissociation due to the Q(3) transition to $2p\pi C^1\Pi_u^-(v' = 13, J' = 3)$. (b) An expanding portion of the left figure for $n = 37$. The area ratios between the peaks of H(2p_{3/2}) and H(2p_{1/2}) for all Rydberg states are listed in Table S1 in the Supplemental Material [32].

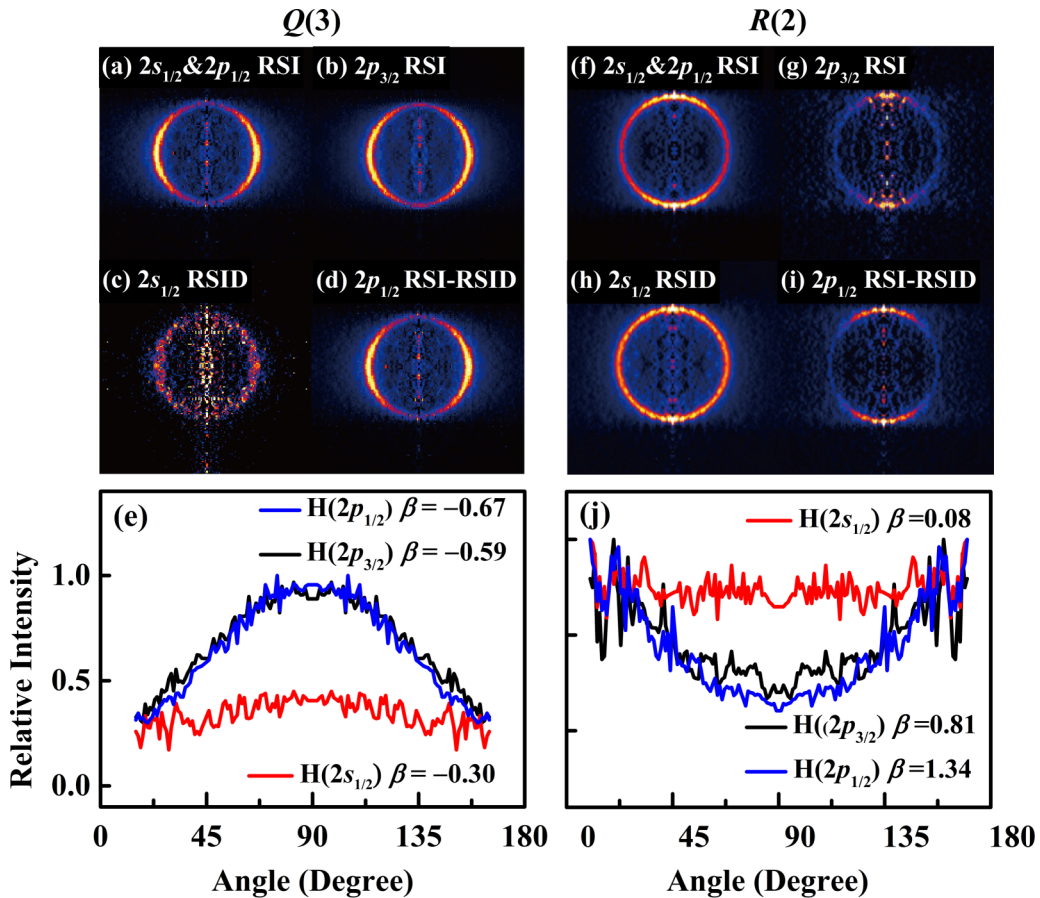


FIG. 9. Inverse-Abel transforms of the velocity map images and the corresponding angular distributions of the H(2s_{1/2}, 2p_{1/2}), H(2p_{3/2}) and H(2s_{1/2}) fragments produced from the predissociations due to the Q(3) and R(2) transitions to $2p\pi C^1\Pi_u^{\pm}(v' = 13)$, respectively. The H(2l) fragments were detected using the RSI and RSID methods by pumping H(2l) to H(n = 52) or H(n = 51). The polarization of the XUV laser is along the up-down direction of the images. The β values are also listed in Table I.

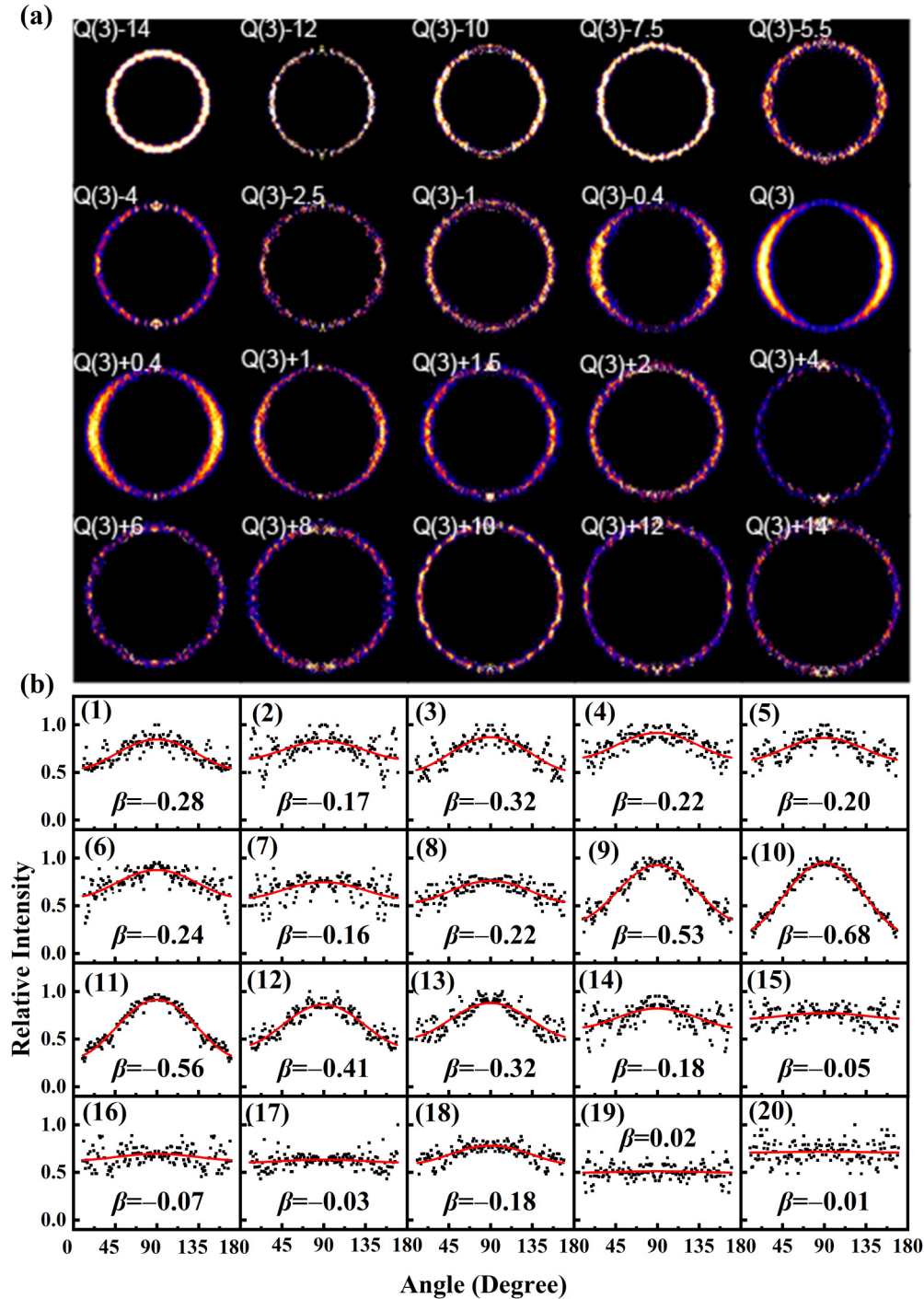


FIG. 10. (a) Inverse-Abel transforms of velocity map images of the H($2l$) fragments along the line profile of the $Q(3)$ transition to $2p\pi C^1\Pi_u^-(v' = 13)$ measured under the electric field. The numbers in the figure indicate the shifts to the line center of the transition; (b) the corresponding angular distributions of the images. The β values are listed in Table S2 in the Supplemental Material [32]; see also Fig. 11.

First, the β value due to the continuum state (β_c) should be taken into consideration. Interference effects between the bound and continuum states also play an important role in determining the angular distribution (β_{int}). The β profile is found to be asymmetrical when the anisotropy parameter due to the continuum state (β_c) is not equal to that due to the interference (β_{int}) ($\beta_c \neq \beta_{\text{int}}$) [24]. Note that the extremum

β in the β profile is located near the Fano dip [21,24]. In the absence of state interference in the Franck-Condon region, the extremum β is located at the line center, and the β profile is symmetrical (see Eq. (9c) in [20] or Eq. (3) in Ref. [24]).

Figure 10 shows the inverse-Abel transforms of the velocity map images of the H($2l$) fragments and the corresponding

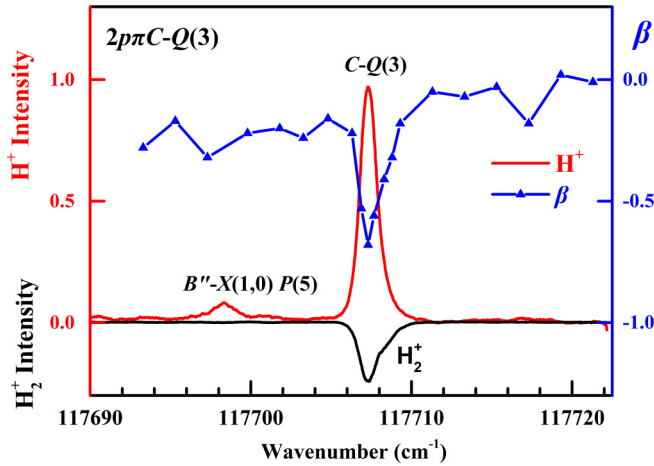


FIG. 11. Anisotropy parameters β of the $H(2l)$ photofragments along the Fano profile of the $Q(3)$ transition to $2p\pi C^1\Pi_u^-(v' = 13)$. The symmetric β profile indicates that the excitation process only involves the $2p\pi C^1\Pi_u^-$ state in the Franck-Condon region.

angular distributions at different excitation energies along the $Q(3)$ line profile. The corresponding β profile is shown in Fig. 11. The experiments were performed under the electric field, and the $H(2s)$ and $H(2p)$ fragments were thus fully mixed [29]. As can be seen, the β profile is almost symmetrical relative to the resonance center, which indicates that the coupling of the $2p\pi C^1\Pi_u^-(v' = 13)$ state with other states is weak in the Franck-Condon region. The β value at the resonance center is -0.68 , which is in agreement with the theoretical calculation. It is surprising to see that the β values for the two sides of the β profile are ~ 0.0 . The transitions outside the resonance peak should be mainly to continuum states, which can be regarded as a combination of $P(3)$, $Q(3)$, and $R(3)$ rotational branches. For the $R(3)$ and $P(3)$ transitions of $^1\Sigma_u^+$ ($^1\Pi_u$) symmetry, the β values should be 0.71 (0.61) and 0.29 (0.14), respectively, which are all positive values larger than 0.0 . Therefore, near-zero β values suggest that the $Q(3)$ branch dominates the transition in the continuum state. Furthermore, more $P(3)$ [$R(3)$] components are expected on the left (right) side of the resonance peak, and β values are thus lower on the left side and higher on the right side, as shown in Fig. 11. The excited continuum state should be the vibrational continuum of the $2p\pi C^1\Pi_u^-$ state in this energy region.

We also measured the β profile for the $R(2)$ transition. Figure 12 shows the inverse-Abel transforms of the $H(2l)$ fragment velocity map images and the corresponding angular distributions along the $R(2)$ line profile. The β profile is shown in Fig. 13. It is seen that the β profile is highly asymmetrical, which indicates that the $2p\pi C^1\Pi_u^+(v' = 13)$ state is coupled with continuum states in the Franck-Condon region [20–25]. Note that the β values vary quickly from positive to negative values as excitation energies decrease from the center of the peak. The reason is not clear to us and should be studied in the future.

In the neighborhood of the $R(2)$ transition, there are three resonances due to the $P(1)$ and $R(1)$ transitions to the $3p\sigma B'^1\Sigma_u^+(v' = 6)$ state and the $R(0)$ transition to the $2p\sigma B'^1\Sigma_u^+(v' = 34)$ state. The three states have lower en-

ergies than the threshold. The peaks of H^+ signals for the three transitions are, in fact, from the two-photon dissociative ionization of H_2^* , which resulted in background signals in the velocity map images and lowered their β values, which we denoted as “*” in the figure.

IV. DISCUSSION

A. $P(3)$, $R(1)$ and $Q(2)$ predissociations

The $P(3)$ and $R(1)$ transitions are to the $2p\pi C^1\Pi_u^+(v' = 13, J' = 2)$ state. There is an L -uncoupling between the $2p\pi C^1\Pi_u^+$ and $2p\sigma B^1\Sigma_u^+$ states [2,29], which results in the predissociation of the $^1\Pi_u^+$ state via the $2p\sigma B^1\Sigma_u^+$ state. Therefore, the dissociation of the $^1\Pi_u^+$ state can occur via both tunneling and coupling with the $2p\sigma B^1\Sigma_u^+$ state. However, the $2p\pi C^1\Pi_u^+(v' = 13, J' = 2)$ state is just $\sim 0.3 \text{ cm}^{-1}$ above the threshold to produce the excited $H(2p_{3/2})$ atoms; the probability of tunneling dissociation is expected to be weak. Our experimental results support such a conclusion: Only the ground state $H(2p_{1/2})$ was observed; therefore, the predissociation of the $2p\pi C^1\Pi_u^+(v' = 13, J' = 2)$ state is a typical single isolated Feshbach resonance [3].

For the $Q(2)$ transition to the $2p\pi C^1\Pi_u^-(v' = 13, J' = 2)$ state, only $H(2p_{1/2})$ was observed, and the linewidth is 0.57 cm^{-1} , similar to that of the $2p\pi C^1\Pi_u^+$ state. It is thus concluded that the tunneling dissociation is weak. Note that the $2p\pi C^1\Pi_u^-$ state does not interact with any singlet state correlating to the channel $H(1s) + H(2p_{1/2})$. The only possible mechanism to produce $H(2p_{1/2})$ is that the $2p\pi C^1\Pi_u^-$ state interacts with some triplet state, possibly $2p\pi C^3\Pi_u^-$, near the dissociation limit via the spin-orbit interaction. The detailed mechanism should be studied in the future.

B. $Q(3)$ and $R(2)$ predissociations

The $Q(3)$ and $R(2)$ transitions are to the $2p\pi C^1\Pi_u^-$ and $2p\pi C^1\Pi_u^+$ states of $v' = 13, J' = 3$, respectively. The energy difference between the two opposite symmetrical states is 1.4 cm^{-1} .

The spin-orbit branching ratio $[H(2p_{3/2})]/[H(2p_{3/2}) + H(2p_{1/2})]$ for the $Q(3)$ transition was found to be 0.63 ± 0.03 , approaching the diabatic limit of $2/3$. The same results have been found in the tunneling dissociation of D_2 [11]. Note that the available kinetic energies of the fragments are $\sim 36 \text{ cm}^{-1}$, which is much larger than the spin-orbit splitting between the $H(2p_{1/2})$ and $H(2p_{3/2})$ states. Therefore, the spin-orbit state distribution can be described by the diabatic model. It may also be concluded that the dissociation occurs via two pathways, tunneling and spin-orbit coupling between $2p\pi C^1\Pi_u^-$ and a triplet state near the dissociation limit.

As we mentioned, the β profile of the $Q(3)$ transition indicates that the predissociation occurs mainly via the $2p\pi C^1\Pi_u^-$ state and the coupling with other states is not important in the Franck-Condon region.

For the $R(2)$ transition, there is a large proportion of $H(2s)$ products, which indicates that there are direct and indirect couplings between $2p\pi C^1\Pi_u^+$ and $3p\sigma B'^1\Sigma_u^+$. The spin-orbit-resolved β parameters clearly showed that the dissociative

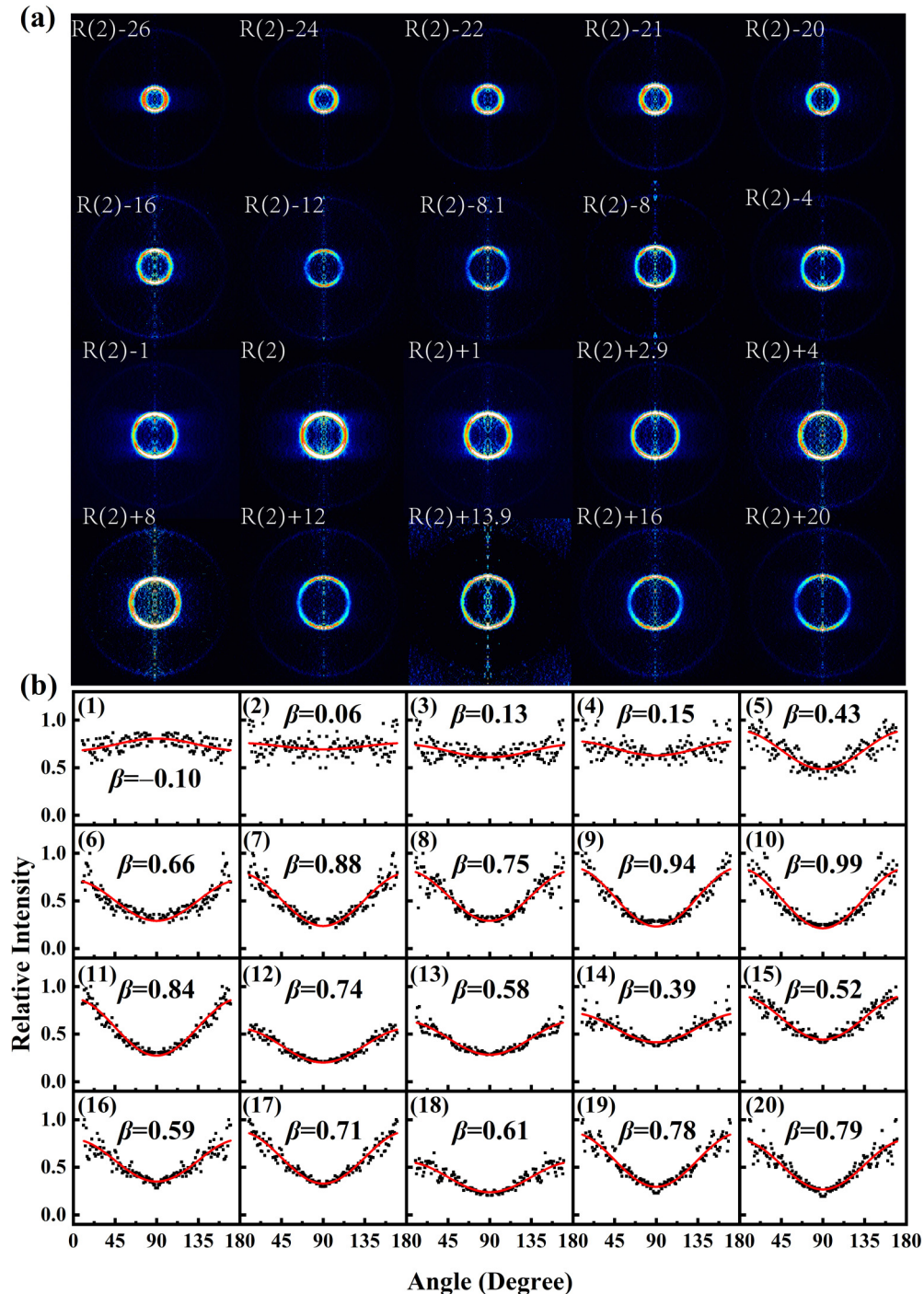


FIG. 12. See the caption of Fig. 10, however, for the $R(2)$ transition to $2p\pi C^1\Pi_u^+(\nu = 13)$. The β values are listed in Table S2 in the Supplemental Material [32]; see also Fig. 13.

states have $^1\Sigma_u^+$ symmetry in the Franck-Condon region. As we mentioned, we could not obtain definite values of the spin-orbit branching ratio between $H(2p_{1/2})$ and $H(2p_{3/2})$ due to the strong $H(2s)$ signals. However, our previous results on the tunneling dissociation of D_2 suggest that the ratio should approach the diabatic limit. The asymmetrical β profile also clearly demonstrates the coupling effect with the $^1\Sigma_u^+$ states. For the predissociation of the $2p\pi C^1\Pi_u^+(\nu = 13, J' = 3)$ state, it can be concluded that there are three dissociation channels: tunneling dissociation producing $H(2p_{1/2})$, and Fe-

sbach resonances producing $H(2s)$ and $H(2p_{3/2})$ by coupling with $2p\sigma B^1\Sigma_u^+$ and $3p\sigma B^1\Sigma_u^+$, respectively. The three dissociation channels should result in a larger linewidth than the previous theoretical results ($<0.1 \text{ cm}^{-1}$) [15].

V. SUMMARY AND OUTLOOK

There is a barrier in the potential energy curve of the $2p\pi C^1\Pi_u$ state of H_2 , which hosts several rotational states [4,12–17]. The previously reported rotational spectra were

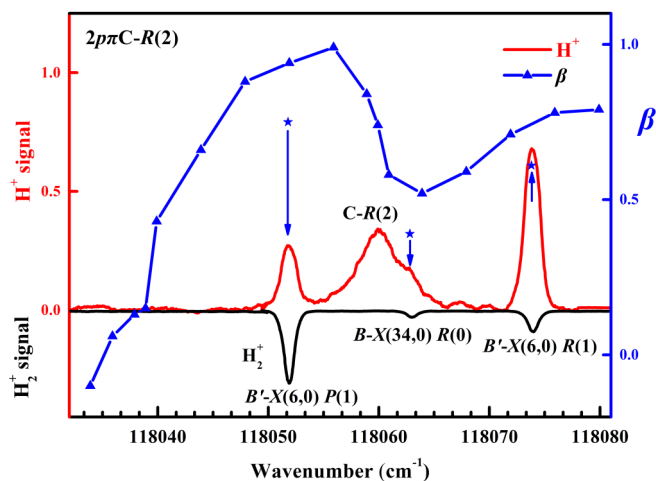


FIG. 13. Anisotropy parameters β of the photofragments $H(2l)$ along the line profile of the $R(2)$ transition to $2p\pi C^1\Pi_u^+(\nu' = 13)$. Note that the β profile is highly asymmetrical showing state interference in the dissociation. Assignments for the transitions of $B'-X(6,0)P(1)$, $B-X(34,0)R(0)$, and $B'-X(6,0)R(1)$ are from Refs. [12,13].

blended due to the rotational transitions of other electronic states [4]. We obtained the rotationally resolved spectra by measuring the components of the blended spectra and deducting the blurred effect.

We also studied the dissociation dynamics by measuring the spin-orbit branching ratios between $H(2p_{1/2})$ and $H(2p_{3/2})$ and the angular distributions of the $H(2l)$ fragments. The $2p\pi C^1\Pi_u^+(\nu' = 13, J' = 2)$ state is 0.7 cm^{-1} above the dissociation threshold, and only the $H(2p_{1/2})$ component (Feshbach resonance) was observed. For the $2p\pi C^1\Pi_u^-(\nu' = 13, J' = 3)$ state where the available kinetic energy is 36 cm^{-1} , the branching ratio $[H(2p_{3/2})]/[H(2p_{1/2}) + H(2p_{3/2})]$ (0.63 ± 0.03) was found

to be close to the diabatic limit, and the measured β profile for the $Q(3)$ transition is symmetrical. It is therefore concluded that the predissociation occurs via the tunneling dissociation and coupling with a triplet state near the dissociation limit. For the $2p\pi C^1\Pi_u^+(\nu' = 13, J' = 3)$ state, the experimental results demonstrated that the predissociation occurs via tunneling, and coupling with the $3p\sigma B'^1\Sigma_u^+$ and $2p\sigma B^1\Sigma_u^+$ states.

The experimental results in this work call for future theoretical studies on some of our interesting findings. For example, to understand the branching ratios between the $H(2p_{1/2})$ and $H(2p_{3/2})$ states produced by the predissociation of the $2p\pi C^1\Pi_u^-$ state, a thorough study is required on the spin-orbit couplings between singlet and triplet states near the dissociation limit. The variation in the β parameters around the resonance peaks (Figs. 11 and 13) may need theoretical calculations considering multichannel couplings.

It is also worth noting that hyperfine structures are rarely considered in the study of molecular photodissociation because of the small energy splittings in comparison with the electronic spin-orbit splittings and translational energies of the fragments. However, we measured the population distributions of the $H(2p_{1/2})$ and $H(2s_{1/2})$ states with an energy spacing of 0.035 cm^{-1} , which is even smaller than the hyperfine level splitting (0.046 cm^{-1}) of the $H(1s_{1/2}, F = 0, 1)$ atom [36]. It would be interesting to measure the population distribution in the hyperfine levels of $H(1s)$ atoms in the future.

ACKNOWLEDGMENTS

This work is funded by Projects No. 21833003 and No. 21773134, supported by the National Natural Science Foundation of China, and by Grant No. 2018YFA0306504, supported by the National Key R&D Program of China.

- [1] H. Kato and M. Baba, Dynamics of excited molecules: Predissociation, *Chem. Rev.* **95**, 2311 (1995).
- [2] H. Lefebvre-Brion and R. W. Field, *The Spectra and Dynamics of Diatomic Molecules: Revised and Enlarged Edition* (Academic Press, New York, 2004).
- [3] H. Friedrich, *Scattering Theory* (Springer-Verlag, Berlin, 2016).
- [4] C. H. Cheng, J. T. Kim, E. E. Eyler, and N. Melikechi, Line shapes and decay dynamics of dissociative resonances above the second dissociation limit of molecular hydrogen, *Phys. Rev. A* **57**, 949 (1998).
- [5] A. de Lange, G. D. Dickenson, E. J. Salumbides, W. Ubachs, N. de Oliveira, D. Joyeux, and L. Nahon, VUV Fourier-transform absorption study of the Lyman and Werner bands in D_2 , *J. Chem. Phys.* **136**, 234310 (2012).
- [6] E. E. Eyler and N. Melikechi, Near-threshold continuum structure and the dissociation energies of H_2 , HD, and D_2 , *Phys. Rev. A* **48**, R18 (1993).
- [7] A. Balakrishnan, V. Smith, and B. P. Stoichelf, Dissociation Energy of the Hydrogen Molecule, *Phys. Rev. Lett.* **68**, 2149 (1992).
- [8] Y. P. Zhang, C. H. Cheng, J. T. Kim, J. Stanojevic, and E. E. Eyler, Dissociation Energies of Molecular Hydrogen and the Molecular Hydrogen Ion, *Phys. Rev. Lett.* **92**, 203003 (2004).
- [9] Y. P. Zhang, J. P. Song, C. L. Gan, X. A. Yan, Z. Q. Nie, T. Jiang, L. Li, K. Du, X. C. Zhang, K. Q. Lu, and E. E. Eyler, The second dissociation threshold bound levels of hydrogen molecule, *Chin. Phys.* **15**, 2288 (2006).
- [10] J. Wang, Q. Meng, and Y. Mo, Electronic and tunneling predissociations in the $2p\pi C^1\Pi_u^\pm(\nu = 19)$ and $3p\pi D^1\Pi_u^\pm(\nu = 4, 5)$ states of D_2 studied by a combination of XUV laser and velocity map imaging, *J. Phys. Chem. A* **121**, 5785 (2017).
- [11] J. Wang and Y. Mo, Predissociation dynamics of $D_2 + h\nu \rightarrow D(1s_{1/2}) + D(2p_{1/2,3/2}, 2s_{1/2})$ revealed by the spin-orbit state resolved fragment branching ratios and angular distributions, *J. Chem. Phys.* **150**, 144306 (2019).
- [12] A. Monfils, The absorption spectra of the molecules H_2 , HD, and D_2 : Part VI. Rotational analysis of the B' , B'' , D , D' , and D'' states, *J. Mol. Spectrosc.* **15**, 265 (1965).

- [13] T. Namioka, Absorption spectra of H₂ in the vacuum-ultraviolet region I. The Lyman and the Werner bands, *J. Chem. Phys.* **40**, 3154 (1964).
- [14] G. Herzberg, The dissociation of hydrogen molecule, *J. Mol. Spectrosc.* **33**, 147 (1970).
- [15] L. Wolniewicz and K. Dressler, The $B^1\Sigma_u^+$, $B'^1\Sigma_u^+$, $C^1\Pi_u$, and $D^1\Pi_u$ states of the H₂ molecule. Matrix elements of angular and radial nonadiabatic coupling and improved *ab initio* potential energy curves, *J. Chem. Phys.* **88**, 3861 (1988).
- [16] J. R. Burciaga and A. L. Ford, Nonadiabatic perturbation of the C state shape resonances in the photodissociation of molecular hydrogen, *J. Mol. Spectrosc.* **149**, 1 (1991).
- [17] J. Abgrall, E. Roueef, and F. Launay, The Lyman and Werner band systems of molecular hydrogen, *J. Mol. Spectrosc.* **157**, 512 (1993).
- [18] A. de Lange, E. Reinhold, and W. Ubachs, Phenomena of *g*-*u* symmetry breakdown in HD, *Int. Rev. Phys. Chem.* **21**, 257 (2002).
- [19] M. Glass-Maujean, Ch. Jungen, M. Roudjane, and W.-Ü L. Tchchang-Brillet, Theory of vibronic interactions in D₂ and H₂: A comparison between multichannel-quantum-defect and coupled-equation approaches, *J. Chem. Phys.* **134**, 204305 (2011).
- [20] M. Glass-Maujean and L. D. A. Siebbeles, Angular distribution of photofragments along a Fano profile, *Phys. Rev. A* **44**, 1577 (1991).
- [21] L. D. A. Siebbeles and M. Glass-Maujean, Polarization of atomic photofragment fluorescence for excitation along a Fano profile: A quantum-mechanical study, *J. Chem. Phys.* **101**, 1019 (1994).
- [22] H. Kim, K. S. Dooley, S. W. North, G. E. Hall, and P. L. Houston, Anisotropy of photofragment recoil as a function of dissociation lifetime, excitation frequency, rotational level, and rotational constant, *J. Chem. Phys.* **125**, 133316 (2006).
- [23] Q. Meng, J. Wang, and Y. Mo, Angle-resolved Beutler-Fano profile and dynamics for the predissociation of H₂, *Phys. Rev. A* **93**, 050501(R) (2016).
- [24] J. Wang and Y. Mo, Asymmetry profiles of the fragment anisotropy parameters along the Fano resonances in the photodissociation of H₂, *Phys. Rev. A* **102**, 050803(R) (2020).
- [25] J. Wang and Y. Mo, Angle-resolved line profiles in the predissociation of D₂: A summation of Fano and Lorentzian profiles, *Phys. Rev. A* **105**, 023102 (2022).
- [26] Q. Meng and Y. Mo, Predissociation dynamics in the $3p\pi D(\nu = 3)$ and $4p\sigma(\nu = 1)$ states of H₂ revealed by product branching ratios and fragment angular distributions, *J. Chem. Phys.* **144**, 154305 (2016).
- [27] J. Wang, Q. Meng, and Y. Mo, Oscillation of Branching Ratios between the $D(2s) + D(1s)$ and the $D(2p) + D(1s)$ Channels in Direct Photodissociation of D₂, *Phys. Rev. Lett.* **119**, 053002 (2017).
- [28] A. T. J. B. Eppink and D. H. Parker, Velocity map imaging of ions and electrons using electrostatic lenses: Application in photoelectron and photofragment ion imaging of molecular oxygen, *Rev. Sci. Instrum.* **68**, 3477 (1997).
- [29] J. E. Mentall and P. M. Guyon, $H(2s)$ and $H(2p)$ branching ratio in the photodissociation of H₂ near threshold, *J. Chem. Phys.* **67**, 3845 (1977).
- [30] R. N. Zare and D. R. Herschbach, Doppler line shape of atomic fluorescence excited by molecular photodissociation, *Proc. IEEE* **51**, 173 (1963).
- [31] U. Fano, Effects of configuration interaction on intensities and phase shifts, *Phys. Rev.* **124**, 1866 (1961).
- [32] See Supplemental Material at <http://link.aps.org/supplemental/10.1103/PhysRevA.106.012824> for H₂ excitation spectrum near the $P(3)$ transition and the tables listing branching ratios $[H(2p_{3/2})]/[H(2p_{3/2}) + H(2p_{1/2})]$ for each peak in Fig. 8 and anisotropy parameters shown in Figs. 11 and 13, respectively.
- [33] K. Mueller-Dethlefs and E. W. Schlag, High resolution zero kinetic energy (ZEKE) photoelectron spectroscopy of molecular systems, *Annu. Rev. Phys. Chem.* **42**, 109 (1991).
- [34] Y. Mo, J. Yang, and G. Chen, Zero kinetic energy photoelectron study of SO₂⁺ (X^2A_1) using coherent extreme ultraviolet radiation, *J. Chem. Phys.* **120**, 1263 (2004).
- [35] J. A. Beswick and M. Glass-Maujean, Interference effects on the $H(2p)$ to $H(2s)$ branching ratio in the photodissociation of hydrogen and deuterium, *Phys. Rev. A* **35**, 3339 (1987).
- [36] A. E. Kramida, A critical compilation of experimental data on spectral lines and energy levels of hydrogen, deuterium, and tritium, *At. Data Nucl. Data Tables* **96**, 586 (2010).